Shock-induced subgrain microstructures as possible homogenous sources of hot spots and initiation sites in energetic polycrystals

J. J. Rimoli,* E. Gürses,† and M. Ortiz‡
Division of Engineering and Applied Science, California Institute of Technology, Pasadena, California 91125, USA
(Received 26 October 2009; revised manuscript received 23 December 2009; published 25 January 2010)

The purpose of this work is to assess the feasibility of a *homogeneous*—or defect-free—initiation mechanism for high energetic materials in which initiation is a direct consequence of the heterogeneity of crystal plasticity at the subgrain scale. In order to assess the feasibility of these mechanisms, we develop a multiscale model that explicitly accounts for three scales: (i) the polycrystalline structure at the macroscale, (ii) single-crystal plasticity—including subgrain microstructure formation—at the mesoscale, and (iii) chemical kinetics at the molecular scale. An explicit construction gives the effective or macroscopic behavior of plastically deforming crystals with microstructure, and enables the reconstruction of optimal microstructures from the computed macroscopic averages. An intrinsic feature of the optimal deformation microstructures is the presence of highly localized regions of plastic deformation or slip lines. Temperatures, strain rates, and pressures in these slip lines rise well in excess of the average or macroscopic values. Slip lines thus provide a plentiful supply of likely initiation sites, or hotspots, in defect-free crystals. We have assessed this initiation mechanism by simulating a PETN plate impact experiment and comparing the resulting predictions with experimental pop-plot data. The computed characteristic exponents are in the ballpark of experimental observation.

DOI: 10.1103/PhysRevB.81.014112 PACS number(s): 02.70.−c, 46.15.−x, 61.72.−y, 62.50.−p

I. INTRODUCTION

Initiation in high energetic (HE) explosives such as pentaerythritol-tetranitrate (PETN), cyclotrimethylene-trinitramine (RDX), cyclotetramethylene-tetranitramine (HMX), and triamino-trinitrobenzene (TATB) by means of mechanical loading has often been attributed to the generation of a sufficiently high density of *hot spots* of certain critical sizes, temperatures, and durations.[1–5] At the crystalline scale, initiation in heterogeneous materials may indeed occur due to the interaction of shocks with material heterogeneities such as grain boundaries, defects, voids, and cracks. These interactions may result in high pressures, temperatures, and deformation rates and eventually lead to molecular decomposition and detonation. A number of mechanisms, including the collapse of voids or pores,[2,6] localized adiabatic shear,[7,8] dislocation pile-up avalanches,[9,10] and friction[11,12] have been assessed as possible sources of hot spots (cf. Field, Swallowe, and Heavens[13] and Field *et al.*[14] for overviews). Indeed, defect content is known to influence *sensitivity*, i.e., the ease with which an explosive can be initiated by a shock. For instance, a strong influence of the sensitivity of HMX on void content has been observed experimentally.[15] In addition, the sensitivity of polymer-bonded explosives can be decreased by reducing crystalline and molecular defects such as voids and pores.[16]

However, a number of factors that are also known influence sensitivity are not well-explained by defect-based models of heterogeneous initiation. For instance, coarse-grained explosives are more sensitive at low shock pressures, whereas fine-grained explosives are more sensitive at higher pressures.[17] In addition, a change in the shape of the grains from faceted to more spherical decreases the sensitivity significantly.[18] Furthermore, initiation sensitivity is also observed in defect-free single-crystals of PETN, a type of sensitivity that cannot be described by means of defect-based initiation models. The initiation sensitivity of defect-free crystals is observed to depend strongly on the crystallographic orientation of the shock direction.[19–23] This effect may be attributed to the inherent anisotropy of plastic flow in single-crystals.

The purpose of this work is to assess the feasibility of a *homogeneous*—or defect-free—initiation mechanism in which initiation is a direct consequence of the heterogeneity of crystal plasticity at the subgrain scale. Thus, metallic crystals deformed to large plastic strains are commonly observed to develop characteristic dislocation structures.[24–37] Often these structures consist of roughly parallel arrays of dislocation walls and may be regarded as instances of *sequential lamination*.[38] The size of the microstructure decreases monotonically with increasing deformation, often into the micrometer and submicrometer range[29,33] and with decreasing grain size. The emergence of dislocation structures is known to have a marked influence on the effective behavior of ductile crystals.[27,29,39–42] For instance, the competition between misfit energy, which favors fine microstructure, and the energy carried by the dislocation walls, which favors coarse microstructures, results in classical Hall-Petch scaling.[38,52–54]

In crystals, the formation of dislocation structures of the type just described is the result of *strong latent hardening*, namely, the fact that crystals exhibit substantially higher hardening rates when deforming in multiple slip than when deforming in single slip. This phenomenon may in turn be attributed to the forest hardening mechanism,[44–48] or, in the words of Piercy *et al.*,[49] the fact that "slip lines of the one system experience difficulty in breaking through the active slip lines of the other one." Experimentally, the phenomenon of strong latent hardening was inferred from observed "patchy slip" patterns[49,50] and was quantified by means of specially designed latent hardening experiments.[49] The presence of strong latent hardening implies that the crystal has a clear incentive—in work of deformation terms—to deform in

single slip and avoid multiple slip. More precisely, the work of deformation expended in deforming a crystal into a deformation field composed of regions of single slip is always less than the work or deformation required to attain the same average or macroscopic deformation by multiple slip.

Whereas these observations apply to conventional crystals and specifically to metals, the physical origin of patterning of plastic deformation is ultimately topological, namely, the entanglement of dislocation lines as they move through the plastically deforming crystal, and, hence, it is to be expected that the same mechanism operate in molecular crystals as well. Remarkably, lamellar structures are indeed observed to emerge in molecular dynamics simulations of the response of the energetic molecular crystals to shock loading.[43] These simulations provide a first indication that microstructure formation is indeed an integral part of the inelasticity of high-energy crystals as well. In high-energy explosives, the formation of subgrain deformation microstructures may result in regions where temperature, pressure, deformation, and rate of deformation are much higher than there average macroscopic values. These regions may then effectively act as "hot spots" and contribute to initiation.

In order to assess the feasibility of this mechanism, we develop a multiscale model that explicitly accounts for three scales: (i) the polycrystalline structure at the macroscale, (ii) single-crystal plasticity—including subgrain microstructure formation—at the mesoscale, and (iii) chemical kinetics at the molecular scale. The polycrystalline structure of the material is resolved explicitly by means of finite elements. At the subgrain level, we avail ourselves of a number of material properties from first-principles calculations, including elastic properties, slip systems, critical resolved shear stresses, and others.[51] In addition, plastically deforming crystals are simply assumed to exhibit *infinite latent hardening*,[38,52] i.e., we require the crystal to deform locally in single slip at all material points. However, grains can attain plastic deformations other than single slip—and thus beat the single-slip constraint—by developing fine microstructure.[38,52–57]

From a mathematical modeling point of view, the main challenge is to identify the most efficient microstructures, i.e., those that allow the material to attain a certain deformation with the least expenditure of work. Equivalently, the problem is to determine the microstructures that result in the *softest* possible material response. HE materials pose the additional challenge that the extremes of the deformation field are of primary interest, in addition to their average values. Conventional mean-field models convey no information about local extremes and, therefore, are insufficient for present purposes. Instead, a *two-way multiscale scheme* is required that, in addition to supplying the mean or macroscopic response, also allows the microstructures underlying that mean behavior to be reconstructed *a posteriori* without loss of information.

In problems where microinertia is negligible, the optimal two-way multiscale scheme is known as *relaxation*.[58–60] However, the relaxation of specific material models, i.e., the determination of their optimal microstructures and of the corresponding effective macroscopic behavior, poses an exceedingly challenging mathematical problem. Fortunately, the relaxation of crystal plasticity is known explicitly in the limit of infinitely strong hardening and small deformations. Specifically, Conti and Ortiz[54] have supplied an explicit construction that generates optimal microstructures and a closed form expression for the corresponding effective behavior.

In this work, we rely on this explicit construction in order to account for subgrain microstructure formation in HE materials. Thus, we use the explicit effective behavior representation of Conti and Ortiz[54] as the constitutive model at all quadrature points in the finite-element polycrystalline calculations and their explicit microstructure construction in order to *reconstruct* optimal microstructures *a posteriori* from the computed macroscopic response of the material. A critical feature of those microstructures is that they necessarily contain *slip lines*, i.e., regions of strong shear concentration, which naturally leads to the formation of hot spots. The computed histories of deformation, pressure, and temperature in the slip lines can then be used as boundary conditions in order to drive full-chemistry calculations of small material samples, thus closing the two-way multiscale modeling loop: atomistic $\rightarrow$ subgrain microstructures $\rightarrow$ polycrystals $\rightarrow$ subgrain microstructures $\rightarrow$ atomistic. However, such full-chemistry calculations are challenging in their own right and are well-beyond the scope of the present work. Instead, we resort to a simple single-step Arrhenius depletion law[61,62] in order to evaluate conditions within individual hot spots. Whereas such an oversimplified chemistry model is far from being quantitatively predictive, it nevertheless serves to develop qualitative intuition and to demonstrate the potential for coupling the predictions of the macro and mesoscale models back to chemistry.

For purposes of validation, in Sec. IV we present results of simulations of plate impact experiments of polycrystalline PETN samples and compare them with pop-plot data.[63] The predicted scaling of the pressure *vs.* time-to-detonation relation is in good overall agreement with experimental observation, which demonstrates the ability of the proposed multiscale model to make contact with the macro and device length and time scales.

II. PLASTICITY OF SINGLE-CRYSTALS

We begin by describing an explicit construction due to Conti and Ortiz[54] that supplies the effective macroscopic behavior of single-crystals undergoing monotonic plastic deformation at the subgrain level and allows to reconstruct the microstructures *a posteriori* for purposes of hot spot analysis. Constructions that relax general single-crystal plasticity with strong latent hardening are only known for small-strain linearized kinematics and, consequently, the present work is restricted to that framework.

In order to describe the construction, we consider a representative volume $\Omega \subset \mathbb{R}^3$ of crystal deformed according to a displacement field $u:\Omega \rightarrow \mathbb{R}^3$. Within a linearized-kinematics framework, the local deformation of the crystal is described by the displacement gradient

$$\beta = \nabla u, \tag{1}$$

and the local strain by the symmetric strain tensor

$$\epsilon = \frac{1}{2}(\beta + \beta^T). \tag{2}$$

Plastic deformation in single-crystals is crystallographic in nature and, for monotonic deformations, the plastic deformation tensor, i.e., the permanent deformation that remains after unloading the crystal, admits the representation

$$\beta^p(\gamma) = \sum_{\alpha=1}^{N} \gamma_\alpha s_\alpha \otimes m_\alpha, \tag{3}$$

where $\gamma_\alpha \in \mathbb{R}$ is the slip strain on the α slip system of the crystal, s_α and m_α are the corresponding slip directions and slip-plane normals, respectively, N is the number of slip systems and $\otimes$ denotes the dyadic product of two vectors, i.e., $(a \otimes b)_{ij} = a_i b_j$. The corresponding plastic strain is

$$\epsilon^p(\gamma) = \frac{1}{2}[\beta^p(\gamma) + \beta^{pT}(\gamma)], \tag{4}$$

and the elastic strain follows as

$$\epsilon^e = \epsilon - \epsilon^p(\gamma). \tag{5}$$

Plastic deformations resulting from conservative glide of dislocations are characterized by slip directions contained within the slip plane, i.e., slip directions such that $s_\alpha \cdot m_\alpha = 0$, and, consequently, such plastic deformations are isochoric or volume-preserving. The slip systems of many conventional crystalline materials classes are well-known experimentally. By contrast, the slip systems of molecular crystals are comparatively less well-known.

We shall further idealize the molecular HE crystals of interest as possessing no self-hardening and infinite latent hardening. These idealizations partly owe to necessity—the hardening characteristics of HE materials are for the most part unknown—but are also partly based on experience with conventional crystals, where they suffice to characterize the main observed features of the deformation microstructures.[38,52,53] The behavior of a monotonically deformed crystal possessing no self-hardening and infinite latent hardening is described by a plastic work function of the form

$$W^p(\gamma, \theta) = \begin{cases} \tau_\alpha(\theta)|\gamma_\alpha|, & \text{if } \gamma_\beta = 0 \text{ for all } \beta \neq \alpha, \\ +\infty, & \text{otherwise}, \end{cases} \tag{6}$$

where τ_α is the critical resolved shear stress of the αth slip system of the crystal and θ is the temperature. Evidently, all symmetry-related systems have the same value of τ_α. We also note that, owing to the infinite latent hardening assumption, local deformations other than single-slip deformations of the form

$$\beta^p(\gamma) = \gamma_\alpha s_\alpha \otimes m_\alpha \quad (\text{no sum in } \alpha), \tag{7}$$

are effectively barred. The free-energy density of the crystal is further assumed to be of the form

$$A(\epsilon, \gamma, \theta) = W^p(\gamma, \theta) + \rho c_v \theta[1 - \log(\theta/\theta_0)] + \frac{1}{2} C_{ijkl}(\theta)[\epsilon^e_{ij} - \alpha_{ij}(\theta - \theta_0)][\epsilon^e_{kl} - \alpha_{kl}(\theta - \theta_0)], \tag{8}$$

where ρ is the mass density, c_v is the heat capacity per unit mass at constant volume, θ_0 is a reference temperature, $C_{ijkl}(\theta) = C_{klij}(\theta) = C_{jikl}(\theta) = C_{ijlk}(\theta)$ are the elastic moduli, and α_{ij} the thermal expansion coefficients. Finally, the strain-energy density of a uniformly deformed crystal is

$$W(\epsilon, \theta) = \min_{\gamma \in \mathbb{R}^N} A(\beta, \gamma, \theta). \tag{9}$$

Owing to the assumption of strong latent hardening, the strain-energy density $W(\epsilon, \theta)$ is strongly *nonconvex* in ϵ, with linear growth for single-slip deformations and quadratic growth in all other directions. Strongly nonconvex strain-energy densities such as Eq. (9) result in equilibrium deformations exhibiting fine microstructure. The problem is, therefore, to identify the *optimal microstructures* that relax the material, i.e., that require the least expenditure of work in order to attain a prescribed macroscopic deformation. The resulting effective—or *relaxed*—energy is known to possess some unique properties.[58–60,64] Thus, for instance, the relaxed energy effectively accounts for all possible microstructures (no loss of physics), but is itself stable against further microstructure formation. Conversely, given a stable equilibrium deformation of the relaxed energy, i.e., and energy minimizer, it is always possible to reconstruct an optimal microstructure that gives the macroscopic deformation on average (no loss of information).

Conveniently, the relaxation of crystals described by Eq. (9) is known explicitly in close form, including an explicit microstructure construction that delivers the relaxation.[54] Specifically, it can be shown that, if the crystal has a sufficiently rich set of slip systems, the relaxation is delivered by a laminate of finite order involving local single slip only and matching the macroscopic deformation on average. We recall that a simple laminate is a deformation consisting of two uniform deformation gradients β_1 and β_2 arranged in alternating layers, or *lamellae*. The deformation gradients β_1 and β_2 must be compatible at the interfaces of the laminate. We recall that two uniform deformation gradients β_1 and β_2 are compatible if and only if $\beta_1 - \beta_2$ has rank 1 when regarded as a 3×3 matrix. A sequential laminate is constructed recursively by repeatedly replacing lamellar regions of uniform deformation by simple laminates delivering the same average deformation.

An optimal sequential laminate for crystals exhibiting strong latent hardening and negligible self-hardening may be constructed as follows.[54,65] Suppose that the average

deformation of the crystal β is given. Begin by expressing β in the form

$$\beta = \epsilon^e + \sum_{\alpha=1}^{k} \gamma_\alpha s_\alpha \otimes m_\alpha + \omega, \tag{10}$$

for some $k \leq N$, where $\epsilon^e = \epsilon^{eT}$ is the elastic deformation, $\omega = -\omega^T$ is an infinitesimal rotation, and the slip strains γ_α deliver the minimum in Eq. (9). If $k=0$ or $k=1$, i.e., if the deformation is elastic or involves activity on one single-slip system, then the deformation is uniform and no microstructure is generated. Suppose that $k \geq 2$, i.e., the slip activity involves at least double slip. The corresponding sequential laminate is constructed by recursion on k. Suppose that optimal laminates can be constructed when deformation involves activity on $k-1$ slip systems. Define the deformations

$$\beta_1 = \epsilon^e + \sum_{\alpha=1}^{k-1} \gamma_\alpha s_\alpha \otimes m_\alpha + \omega, \tag{11}$$

and

$$\beta_2 = \beta_1 + \frac{1}{\varepsilon} \gamma_k s_k \otimes m_k, \tag{12}$$

where ε is a small parameter. Evidently, $\beta_2 - \beta_1 = \varepsilon^{-1} \gamma_k s_k \otimes m_k$ and, therefore, β_1 and β_2 are rank 1 connected. In addition, $\beta = (1-\varepsilon)\beta_1 + \varepsilon \beta_2$. Hence, the macroscopic deformation β is delivered on average by a simple laminate supported on the deformations β_1 and β_2 with volume fractions ε and $1-\varepsilon$. The geometry of this laminate is noteworthy. Thus, the lamellar interfaces are coplanar with the slip plane of the kth system. In addition, the laminate involves concentration of deformations on the kth system, i.e., the kth system is active on a very narrow lamellar region whose thickness scales as ε and the corresponding slip strain simultaneously blows up as ε^{-1}. We note that β_1 and β_2 involve activity on $k-1$ and k slip systems, respectively. In order to fully reduce the problem to the case of activity on $k-1$ systems, we introduce the additional deformations

$$\beta_3 = \epsilon^e + \sum_{\alpha=2}^{k-1} \gamma_\alpha s_\alpha \otimes m_\alpha + \frac{1}{\varepsilon} \gamma_k s_k \otimes m_k + \omega, \tag{13}$$

and

$$\beta_4 = \beta_3 + \frac{1}{\varepsilon} \gamma_1 s_1 \otimes m_1. \tag{14}$$

We note that the sum in Eq. (13) starts from $\alpha=2$ (and is understood to be empty if $k=2$) and, hence, β_3 involves activity on $k-1$ slip systems only. In addition $\beta_2 = (1-\varepsilon)\beta_3 + \epsilon \beta_4$ and $\beta_4 - \beta_3 = \varepsilon^{-1} \gamma_1 s_1 \otimes m_1$ is of rank 1. Hence, the β_2 lamellae can be replaced by a simple laminate at deformations β_3 and β_4 with volume fractions $(1-\varepsilon)$ and ε, respectively. The resulting microstructure is shown schematically in Fig. 1 and consists of three variants of deformation at β_1, β_2, and β_3 with weights $(1-\varepsilon)$, $\varepsilon(1-\varepsilon)$, and ε^2, respectively (the software employed in this and subsequent figures for the visualization of sequential laminates is courtesy of M. Fago).[66] By the inductive assumption, β_1 and β_2 can be generated as laminates of single-slip deformation with energies close to $W(\epsilon_1, \theta)$ and $W(\epsilon_2, \theta)$, respectively. The energy carried by the left-over deformation β_4 can be estimated and, owing to the corresponding small volume fraction of order ε^2, it is found to be negligible.

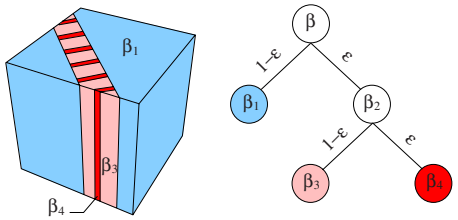

FIG. 1. (Color online) Illustration of the recursive construction of Conti and Ortiz (Ref. 54) for crystals with high latent hardening. Lamellar microstructure resulting from the activation of two slip systems. The macroscopic deformation β first decomposes into deformations β_1 and β_2 consisting of single and double slip, respectively. Subsequently, β_2 further decomposes into deformations β_3 and β_4 involving single and double slip, respectively. The deformation β_4 is highly localized and thus constitutes a potential hot spot. The left figure shows the spatial geometry of the microstructure. The color coding identifies regions of the same uniform deformation. The right figure shows a diagram of the compatibility relations between the various variants of deformation (the nodes of the graph), as well as their respective volume fractions (shown on the links in the graph). Thus, the deformations β_1 and β_2 must be rank-1 compatible and average to the macroscopic deformation β, whereas the deformations β_3 and β_4 must be rank-1 compatible and average to the deformation β_2.

The end conclusion afforded by the above construction is that any macroscopic deformation β can be decomposed into a sequential laminate supported on single-slip deformations and whose energy of is arbitrarily close (as $\varepsilon \to 0$) to the convex envelop $W^{**}(\epsilon, \theta)$ of $W(\epsilon, \theta)$. This limit is optimal, in the sense that the crystal cannot reduce its energy further by means of any other microstructure, and supplies an explicit expression for the effective macroscopic energy of the crystal, namely, the convexification of the unrelaxed energy density $W(\epsilon, \theta)$. We note that, whereas for scalar problems convexification, also known as the Gibbs common-tangent construction, always supplies the relaxation of a nonconvex energy, that is not the case in vectorial problems such as considered here for which, owing to the compatibility or rank 1 constraint, the relaxed energy lies above the convexification of the energy in general. Thus, the conclusion that the relaxation of crystal plasticity coincides with its convexification is a nontrivial result. Physically, the convex envelop $W^{**}(\epsilon, \theta)$ describes ideally plastic multiple slip behavior and, thus, the net effect of relaxation can be loosely described by saying that the formation of optimal deformation microstructures entirely "beats" strong latent hardening.

It should be carefully noted that the optimal microstructure that delivers the relaxed energy is not necessarily unique. In addition, the preceding construction is not necessarily the only one that relaxes the energy. We also note that

TABLE I. The set of slip systems for PETN crystals relative to tetragonal axes.

Slip system	I	II	III	IV	V	VI
Slip direction	$\pm[1\bar{1}1]$	$\pm[1\bar{1}\bar{1}]$	$\pm[111]$	$\pm[11\bar{1}]$	$\pm[1\bar{1}0]$	$\pm[\bar{1}\bar{1}0]$
Plane normal	(110)	(110)	$(1\bar{1}0)$	$(1\bar{1}0)$	(110)	$(1\bar{1}0)$
τ_c (GPa)[a]	1.0	1.0	1.0	1.0	2.0	2.0

[a]Reference 51.

the preceding construction by itself can lead to a multiplicity of microstructures depending on the ordering of the slip systems. In order to partly resolve this source of ambiguity, in calculations we order the systems by slip activity, i.e., we consider first the system or systems that are most active, then the system or systems that are second most active, and so on.

These considerations of nonuniqueness notwithstanding, a common feature of all optimal microstructures is that they must necessarily contain narrow regions of slip concentration or *slip lines*. Indeed, it can be shown[54] that the optimal energy cannot be attained without the development of such slip lines. To restate this result, *the deformation of single-crystals exhibiting strong latent hardening and negligible self-hardening necessarily involves the formation of slip lines at the microscale*. The deformations, rates of deformation, pressures, and temperatures in the slip lines may be expected to reach exceedingly high values. Therefore, in HE materials the slip lines supply likely initiation sites, or *hot spots*, in the absence of extended crystal defects such as voids.

III. CRYSTAL PLASTICITY OF PETN CRYSTALS

We choose PETN as our model HE material for purposes of verifying the feasibility of the slip-line mechanism of hot spot generation described in the foregoing. Unfortunately, there is a paucity of experimental data and theoretical understanding regarding the fundamental mechanisms of plasticity in molecular crystals in general, and PETN in particular. We partly sidestep this difficulty by employing material data obtained from first principles[51] in order to supplement the available experimental data. In this section we collect the PETN data set that is used in the calculations presented in the sequel.

There seems to be general agreement that PETN exhibits plastic slip mainly on {1 10} planes.[67] By contrast, the size and direction of the Burgers vector is open to speculation.[19,68] In calculations we employ the set of slip systems and the corresponding critical resolved shear stresses determined by Xu *et al.*[51] through gamma-surface calculations. These data are collected in Table I and visualized in Fig. 2. The slip systems I–IV are in agreement with x-ray topography and the analysis of slip traces after surface indentation.[67] The remaining slip systems V and VI require higher stresses in order to be activated.

Highly localized and rapid deformations can generate very high temperatures due to conversion of plastic dissipation to heat and adiabatic heating. The rate of plastic dissipation is a crystal is

$$\dot{W}^p = \sum_{\alpha=1}^{N} \tau_\alpha \dot{\gamma}_\alpha. \tag{15}$$

Assuming that a fraction $\eta < 1$ of this plastic work is converted to heat and rate of adiabatic heating is given by

$$\rho c_v \dot{\theta} = \eta \dot{W}^p, \tag{16}$$

which enables the computation of the temperature locally once the slip activity is known. In general, the fraction η of plastic work converted to heat is observed to depend on strain and strain rate.[69–72] However, owing to a lack of data for PETN in calculations we simply use the upper bound $\eta = 1$, i.e., we assume that all the plastic work is converted to heat.

It bears emphasis that the adiabatic temperature rise (16) is computed individually for each of the lamellar regions in the microstructures generated during the plastic working of the crystal. In particular, the temperature in the slip lines may rise greatly in excess of the average temperature of the crystal, which in turn may be expected to strongly influence initiation. The presence of such large local fluctuations again speaks to the need for multiscale models that characterize local extremes in the distribution of temperature, pressure, and deformation, and not just macroscopic averages.

The critical resolved shear stresses are generally observed to exhibit thermal softening and strain-rate dependency.

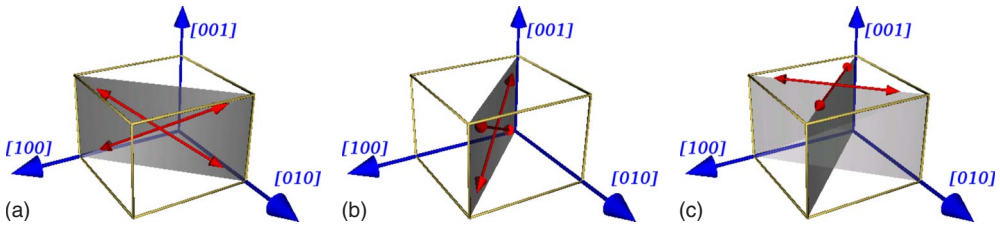

FIG. 2. (Color online) Slip systems of PETN single-crystals.

Assuming thermal activation, the dependence of the critical resolved shear stresses on temperature and slip-strain rate is of the form[73]

$$\tau_\alpha(\dot{\gamma}_\alpha, \theta) = \tau_{\alpha 0}\frac{k_B\theta}{G_\alpha}\text{asinh}\left(\frac{\dot{\gamma}_\alpha}{\dot{\gamma}_{\alpha 0}}e^{G_\alpha/k_B\theta}\right), \tag{17}$$

where k_B is the Boltzmann constant, $\tau_{\alpha 0}$ is the critical resolve shear stress for system α at zero temperature and at the reference slip-strain rate $\dot{\gamma}_{\alpha 0}$ and G_α is an activation energy for system α. We calibrate (17) using the constants in Table I and through fitting to experimental data.[74] We further account for the temperature dependence of the elastic constants simply through a linear relation that interpolates between the value of the elastic constants at 0 K and zero at the melting temperature.

In order to illustrate how the *two-way* multiscale modeling loop—atomistic → subgrain microstructures → polycrystals → subgrain microstructures → atomistic—can be closed, we analyze hot spots for chemical decomposition. Specifically, for each of the lamellar regions in the microstructures generated during the plastic deformation of the crystal we apply a simple Arrhenius-type depletion law[61,62]

$$\frac{d\lambda}{dt} = Z(1-\lambda)\exp\left(-\frac{E}{R\theta}\right), \tag{18}$$

where θ is the local temperature, Z is a kinetic rate constant, E is an activation energy per mol of material, R is the universal gas constant, and $\lambda \in [0,1]$ reaction progress variable, i.e., $\lambda=0$ corresponds to no reaction and $\lambda=1$ represents a complete chemical decomposition. Evidently, a simple one-step empirical model such as Eq. (18) cannot be expected to be predictive. Here we use such a model mainly to illustrate how the local state histories computed from the mesoscale model can be passed down, as boundary conditions, to a full-chemistry model, and to build intuition regarding the effectiveness of the initiation mechanism under consideration.

A compilation of material constants used in calculations is collected in Table II.

TABLE II. Material constants for PETN.

Elastic constants[b]	$C_{11}=17.22\times10^3$ MPa
	$C_{33}=12.17\times10^3$ MPa
	$C_{44}=5.04\times10^3$ MPa
	$C_{66}=3.95\times10^3$ MPa
	$C_{12}=5.44\times10^3$ MPa
	$C_{13}=7.99\times10^3$ MPa
Melting temperature[c]	$\theta_{\text{melt}}=142.9$ °C
CRSS thermal and	$(\tau_c k_B/G)^{I-IV}=0.446$ GPa/K
Softening parameters[a]	$(\tau_c k_B/G)^{I-IV}=0.370$ GPa/K
	$(G/k_B)^{I-IV}=621.88$ K
	$(G/k_B)^{V-VI}=622.00$ K
Density	$\rho=1.778$ g/cm^3
Specific heat[d]	$c_v=1.14\times10^3$ J/kg/K
Taylor-Quinney	$\eta=1.0[-]$
Activation energy[e]	$E=196.742\times10^3$ J/mol
Gas constant	$R=8.314$ J/mol/K
Kinetic rate constant[e]	$Z=6.3\times10^{19}$ s^{-1}

[a]Reference 51.
[b]Reference 75.
[c]Reference 76.
[d]Reference 77.
[e]Reference 78.

IV. NUMERICAL TESTS

We exercise the multiscale model described in the foregoing in a simple plate impact configuration, Fig. 3. Specifically, we consider a target plate of polycrystalline PETN that is impacted on its rear surface by a rigid striker plate. Owing to the nominal uniaxial strain character of the ensuing deformations in the plate, it suffices to consider a computational domain consisting of a prismatic through-thickness core, Fig. 3(a). The effect of the striker plate is simulated through the application of a constant velocity to the rear surface of the target plate. The normal displacements of the through-thickness boundary of the computational domain are constrained so as to simulate infinite-plate geometry. The finite-element mesh used in the simulations is shown in Fig. 3(b). The mesh explicitly resolves the polycrystalline structure of the material, which consists of randomly oriented, roughly equiaxed grains. The dimensions of the sample are $800\times400\times400$ μm and the maximum grain size is 100 μm. The model consists of 817 grains discretized into approximately 270 000 finite elements. The impact velocities

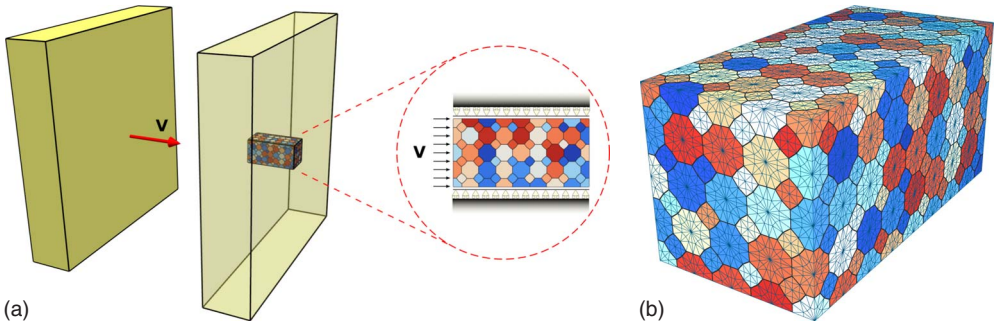

FIG. 3. (Color online) Plate impact test simulation. (a) Definition of computational domain and boundary conditions. (b) Finite-element mesh resolving the polycrystalline structure of the sample.

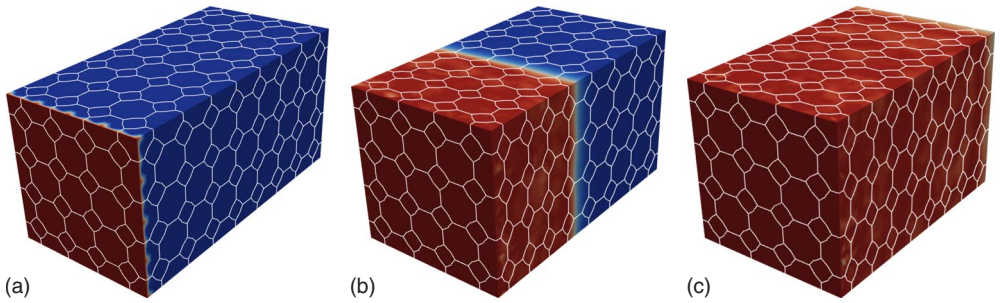

FIG. 4. (Color online) Macroscopic evolution of through-thickness velocity component for an impact velocity of 700 m/s. Red and blue colors in the figure correspond to velocities of 700 m/s and 0 m/s, respectively.

considered in the simulations vary in the range of 500–800 m/s. The calculations are carried out using explicit dynamics with a constant time step $\Delta t = 1 \times 10^{-10}$ s. The simulation is terminated when the planar wave that is induced by the impact traverses the entire thickness of the plate.

Fig. 4 collects several snapshots of through-thickness velocity for an impact velocity of 700 m/s. The red and blue colors in the figure correspond to velocities of 700 and 0 m/s, respectively. As expected, the velocity jumps discontinuously across an ostensibly planar front that propagates through the thickness of the plate. The width of the front profile is commensurate with the mesh size and, in particular, smaller than the grain size. Fig. 5 shows the evolution of the macroscopic temperature for the same impact velocity, which varies in the range of 273–400 K. At material points where deformation microstructures form, the macroscopic temperature follows as the volume average of the microscopic temperature field, which varies sharply on the scale of the microstructure. Grain-to-grain and in-grain fluctuations in the macroscopic temperature field arising as a direct consequence of the polycrystalline microstructure are clearly evident in Fig. 5. However, these macroscopic temperature fluctuations are of modest amplitude and, therefore, unlikely to suffice to cause initiation. By way of contrast, Fig. 6 shows the temperature evolution in a typical subgrain microstructure induced by the plastic working of the grains. As may be observed in the figure, the microscopic distribution of temperature is highly inhomogeneous, with extremely localized peaks occurring within the slip lines in the microstructure. These highly localized peak temperatures are greatly in excess of the average or macroscopic temperature and, therefore, much more likely to cause initiation. It bears emphasis that the temperature extremes are completely missed by mean-field models of plastic deformation and that consideration of subgrain deformation microstructures is key to the prediction of such temperatures. A typical temporal evolution of the temperature and reacted molar fraction within a slip line is shown in Fig. 7. The high maximum temperature of 1000 K is noteworthy, as is the time of 0.015 μs at which chemical decomposition is complete. Finally, Fig. 8 collects statistics of hot spots identified according to several criteria, namely, minimum attained pressure, minimum attained reacted fraction and minimum attained temperature. Again, the high pressures and temperatures attained within some of the hot spots are noteworthy.

Finally, we endeavor to compare the predictions of the model with pop-plot data.[63] This comparison is intended to provide a measure of validation of the model and also to illustrate the ability of the multiscale approach to make contact with full-scale experimental data and applications. Pop plots provide shock initiation data in the form of input pressure *vs.* distance traveled by the shock wave—or, alternatively, time elapsed—to detonation. These data are often presented in the form of log-log plots and are intended to characterize relative sensitivities of high energetic materials. Specifically, the shorter the time-to-initiation the more sensitive the explosive is deemed. In this manner, the influence of the ambient temperature, the pulse length, confinement, and other factors, on the sensitivity of explosives has been systematically studied.[79–81] It is observed in these studies that the log-log plots are almost universally linear for a broad

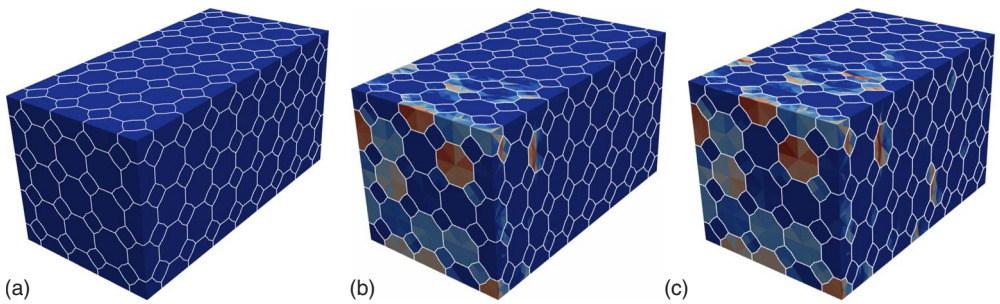

FIG. 5. (Color online) Macroscopic evolution of temperature for an impact velocity of 700 m/s. Red and blue colors in the figure correspond to temperatures of θ=400 K and 273, respectively.

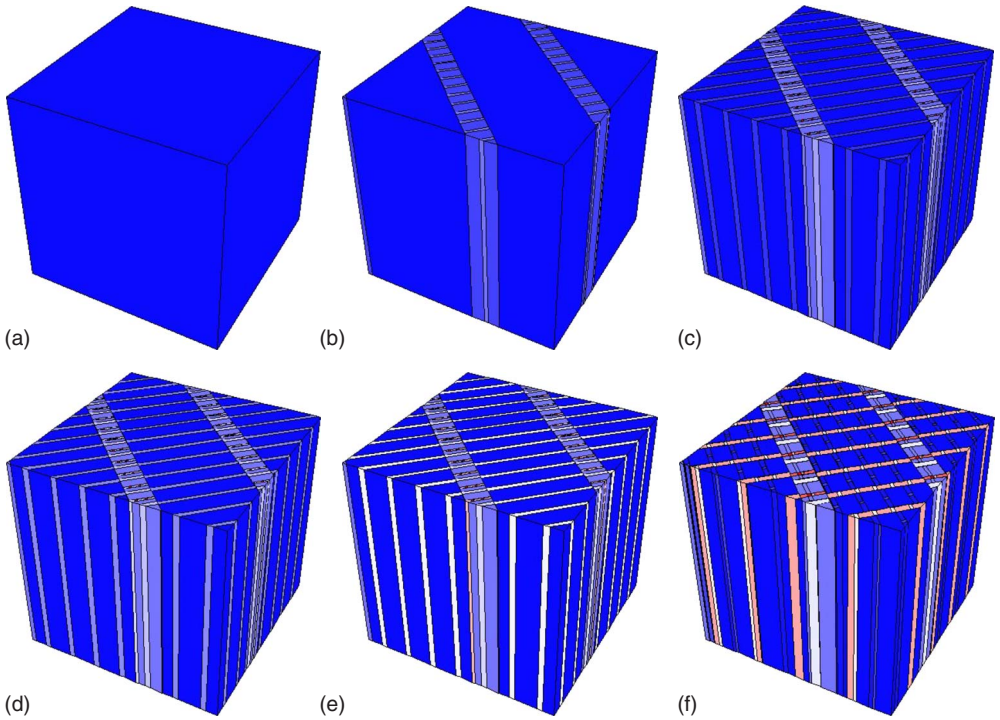

FIG. 6. (Color online) Microscopic evolution of temperature in a typical deformation microstructure at a material (quadrature) point in the finite-element mesh selected at random. The figures show the spatial distribution of deformation in the microstructure. Each lamellar region in the microstructure is uniformly deformed. The deformations between adjacent lamellae are compatible and the overall macroscopic deformation is recovered as the spatial average of the deformations in the lamellae. Coloring encodes temperature, with blue corresponding to the initial temperature of 273 K and maximum temperatures in the range of 1200 K. The monotonic increase of the temperature in regions of highly localized deformation and the increasing complexity of the microstructure are noteworthy.

range of explosives and conditions,[81–84] indicative of a power-law scaling of the shock pressure p with the distance-to-detonation L of the form

$$p = C_p L^{-1/\alpha_p}, \tag{19}$$

where α_p is a characteristic exponent that is given by the slope of the pop-plot curve. In particular, the observed characteristic exponents for PETN vary widely in the range of 1.5–3.5 depending on composition and test conditions.[21,81,83] Low-density PETN (ρ=1.0 g/cm^3) is considerably more sensitive than other variants of PETN and has a characteristic exponent as high as 3.4. This enhanced sensitivity is likely due to the generation of hot spots from voids and other extended defects. By contrast, the characteristic exponents of normal-density PETN (ρ=1.6–1.75 g/cm^3) vary in the lower range of 1.25–1.90.

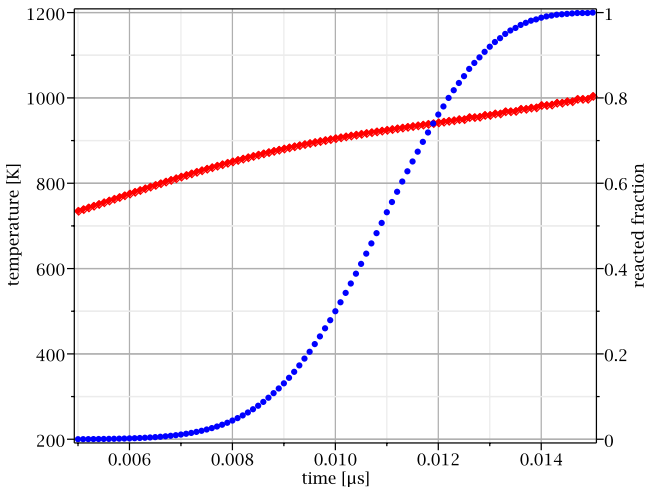

FIG. 7. (Color online) Temperature and reacted fraction evolution in a typical hot spot. Red diamonds and blue circles correspond to the temperature and the reacted fraction, respectively.

We have specifically assessed the ability of the model to predict experimentally observed pop-plot characteristic exponents for PETN. The comparison with experimental data is predicated on the assumption that initiation in a pop-plot test requires the formation of a critical number N_c of hot spots. The number of hot spots N can then be estimated as $N \sim nAL$ where L is the distance traveled by the shock and A is a cross sectional area. Therefore, at the critical number of hot spots we have $L_c \sim N_c/nA$, which is suggestive of an inverse relation between the distance-to-detonation L_c and the density n of hot spots. Thus, a low (respectively, high) impact velocity that generates a low (respectively, high) hot spot density results in a correspondingly large (respectively, small) distance to detonation, as expected. The scaling relation $L_c \sim 1/n$ enables the determination of characteristic exponents α_p from computed hot spot densities, cf. Fig. 8. In order to further facilitate comparisons with experimental data, we resort to shock initiation data[21,79,80,82,84–86] in order to recast the experimental pop plots in terms of impact

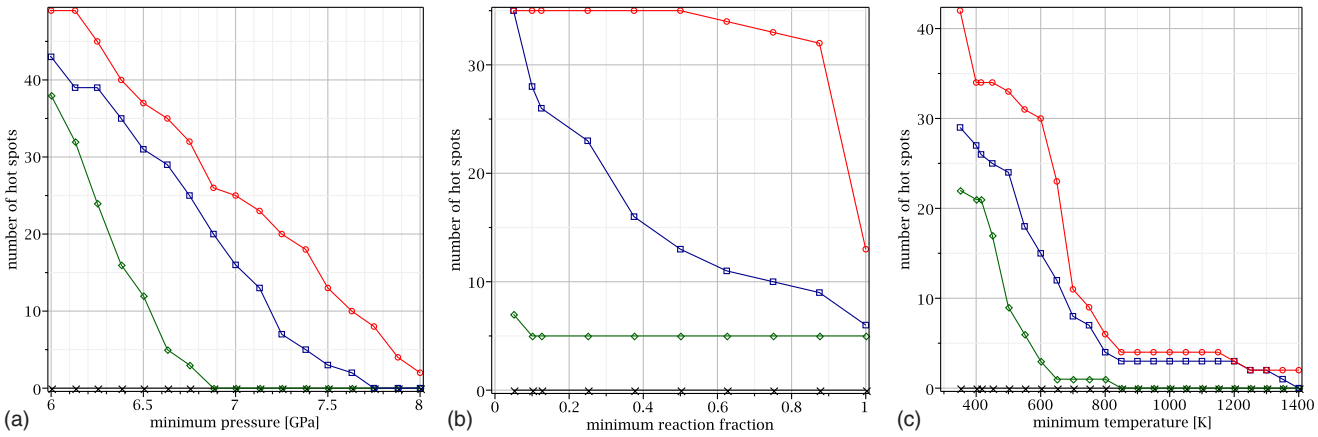

FIG. 8. (Color online) Hot spot statistics for impact velocities of 500 m/s (black cross), 600 m/s (green diamond), 700 m/s (blue box), and 800 m/s (red circle). Hot spots are identified based on the attainment of a minimum pressure, minimum reacted fraction or minimum temperature.

velocity in lieu of pressure. Remarkably, the resulting impact velocity vs distance-to-detonation relation also exhibits power-law behavior of the form

$$V = C_V L^{-1/\alpha_V}. \tag{20}$$

For single-crystal PETN, the characteristic exponent α_V varies in the range of 2.01–2.58.

Fig. 9 shows the pop-plot predicted in the manner just described, with hot spots identified with slip lines that attain a temperature greater than 700 K, a reacted fraction greater than 1% and a pressure greater than 6 GPa.[2,11,14,87] As may be seen from the figure, the pop plot predicted by the model is consistent with power-law scaling, in agreement with experiments.[81,83] The characteristic exponent predicted by the model is 2.91, which slightly overestimates the experimental range of 2.01–2.58 for single-crystal PETN.

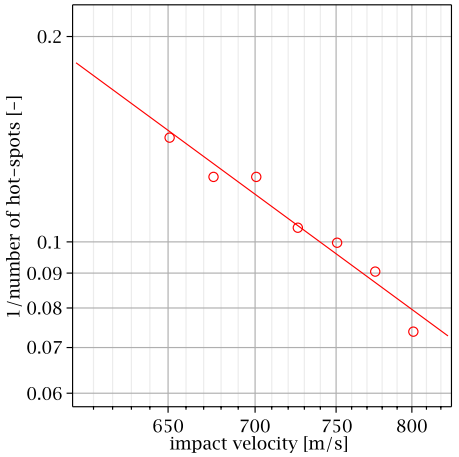

FIG. 9. (Color online) PETN plate impact simulation. Power-law scaling relation between the inverse of number of hot spots and the impact velocity. The circles are the simulation results for different impact velocities. The least square fit to the data shown by the solid line has the slope of 2.91.

V. SUMMARY AND CONCLUSIONS

We have developed a multiscale model that explicitly accounts for three scales: (i) the polycrystalline structure at the macroscale, (ii) single-crystal plasticity—including subgrain microstructure formation—at the mesoscale and (iii) chemical kinetics at the molecular scale. The centerpiece of the model is an explicit construction that: (i) gives the effective or macroscopic behavior of plastically deforming crystals with microstructure and (ii) enables the reconstruction of optimal microstructures from the computed macroscopic averages.[38,52–57] An intrinsic feature of the deformation microstructures that arise in plastically worked crystals is the presence of highly localized regions of plastic deformation, or slip lines. The temperatures, strain rates, and pressures in these slip lines rise well in excess of the average or macroscopic values. Slip lines thus provide a plentiful supply of likely initiation sites, or hot spots, in defect-free crystals. We have assessed the feasibility of the slip-line initiation mechanism by simulating a PETN plate impact experiment and comparing the resulting predictions with experimental pop-plot data. The computed characteristic exponents are in the ballpark of observation, which furnishes a modicum of validation of the model and illustrates the ability of the multiscale model to make contact with full-scale experimental data and applications.

We close by pointing out the rudimentary degree of development of dislocation mechanics and crystal plasticity for molecular crystals in general, and HE materials in particular. Regrettably, this lack of development necessarily limits our present ability to formulate physics-based multiscale models for such materials. Indeed, it appears that precious little is known, either theoretically or experimentally, about fundamental properties of molecular-crystal dislocations such as core structures, core energies and dislocation mobility. The lack of present knowledge about fundamental properties of molecular-crystal plasticity, such as hardening rates, thermal softening and rate sensitivity is equally vexing. The removal of these glaring gaps in our knowledge clearly lies in the critical path of any comprehensive effort to develop predictive, physics based, models of HE initiation, and sensitivity.

ACKNOWLEDGMENTS

We gratefully acknowledge support from the Army Research Office through the MURI on *The Fundamental Chemistry and Physics of Munitions Under Extreme Conditions*, Grant No. W911NF-05-1-0345. We are grateful to Betsy M. Rice and Peter Chung of the Army Research Laboratory for kindly referring us to test data and to Thomas D. Sewell of the University of Missouri-Columbia for many useful discussions.

*jjr@caltech.edu
†gurses@caltech.edu
‡ortiz@aero.caltech.edu

[1] F. P. Bowden, M. A. Stone, and G. K. Tudor, Proc. R. Soc. London, Ser. A **188**, 329 (1947).
[2] F. P. Bowden and A. D. Yoffe, *Initiation and Growth of Explosives in Liquids and Solids* (Cambridge University Press, Cambridge, 1952).
[3] R. W. Armstrong and W. L. Elban, Mater. Sci. Technol. **22**, 381 (2006).
[4] S. M. Walley, J. Field, and M. W. Greenaway, Mater. Sci. Technol. **22**, 402 (2006).
[5] B. M. Rice and T. D. Sewell, in *Static Compression of Energetic Materials*, edited by S. Peiris and G. Piermarini (Springer-Verlag, Berlin, 2008), Chap. 7, pp. 255–290.
[6] M. M. Chaudhri and J. E. Field, Proc. R. Soc. London, Ser. A **340**, 113 (1974).
[7] G. T. Afanas'ev, V. K. Bobolev, Y. A. Kazarova, and Y. F. Karabanov, Combust., Explos. Shock Waves **8**, 241 (1972).
[8] R. E. Winter and J. E. Field, Proc. R. Soc. London, Ser. A **343**, 399 (1975).
[9] C. S. Coffey, Phys. Rev. B **24**, 6984 (1981).
[10] R. W. Armstrong, C. S. Coffey, and W. L. Elban, Acta Metall. **30**, 2111 (1982).
[11] F. P. Bowden and O. A. Gurton, Proc. R. Soc. London, Ser. A **198**, 337 (1949).
[12] M. M. Chaudhri, Nature (London) **263**, 121 (1976).
[13] J. E. Field, G. M. Swallowe, and S. N. Heavens, Proc. R. Soc. London, Ser. A **382**, 231 (1982).
[14] J. E. Field, N. K. Bourne, S. J. P. Plamer, and S. M. Walley, Philos. Trans. R. Soc. London, Ser. A **339**, 269 (1992).
[15] R. L. Gustavsen, S. A. Sheffield, R. R. Alcon, L. G. Hill, R. E. Winter, D. A. Salisbury, and P. Taylor, in *Shock Compression of Condensed Matter*, AIP Conf. Proc. No. 505, edited by M. N. Furnish, L. C. Chhabildas, and R. S. Hixon (AIP, New York, 2000), pp. 879–882.
[16] A. E. D. M. van der Heijden, R. H. B. Bouma, and A. C. van der Steen, Propellants, Explos., Pyrotech. **29**, 304 (2004).
[17] H. Moulard, Proceedings of the Ninth International Detonation Symposium 1989 (unpublished), pp. 902–913.
[18] A. E. D. M. van der Heijden and R. H. B. Bouma, Cryst. Growth Des. **4**, 999 (2004).
[19] J. J. Dick, Appl. Phys. Lett. **44**, 859 (1984).
[20] J. J. Dick, J. Appl. Phys. **81**, 601 (1997).
[21] J. J. Dick, R. N. Mulford, W. J. Spencer, D. R. Pettit, E. Garcia, and D. C. Shaw, J. Appl. Phys. **70**, 3572 (1991).
[22] J. J. Dick and J. P. Ritchie, J. Appl. Phys. **76**, 2726 (1994).
[23] C. S. Yoo, N. C. Holmes, P. C. Souers, F. H. Wu, C. J. Ree, and J. J. Dick, J. Appl. Phys. **88**, 70 (2000).
[24] D. A. Hughes and N. Hansen, Mater. Sci. Technol. **7**, 544 (1991).
[25] N. Hansen, Scr. Metall. Mater. **27**, 1447 (1992).
[26] B. Bay, N. Hansen, D. Hughes, and D. Kuhlmann-Wilsdorf, Acta Metall. Mater. **40**, 205 (1992).
[27] D. A. Hughes and N. Hansen, Metall. Trans. A **24**, 2022 (1993).
[28] D. Hughes, D. Dawson, J. Korellis, and L. Weingarten, J. Mater. Eng. Perform. **3**, 459 (1994).
[29] N. Hansen and D. Hughes, Phys. Status Solidi A **149**, 155 (1995).
[30] D. Hughes and N. Hansen, Scr. Metall. Mater. **33**, 315 (1995).
[31] G. Rosen, D. Jensen, D. Hughes, and N. Hansen, Acta Metall. Mater. **43**, 2563 (1995).
[32] D. Hughes, Q. Liu, D. Chrzan, and N. Hansen, Acta Mater. **45**, 105 (1997).
[33] D. Hughes and N. Hansen, Acta Mater. **45**, 3871 (1997).
[34] L. E. Murr, M. A. Meyers, C.-S. Niou, Y. J. Chen, S. Pappu, and C. Kennedy, Acta Mater. **45**, 157 (1997).
[35] V. Nesterenko, M. Meyers, J. LaSalvia, M. Bondar, Y. Chen, and Y. Lukyanov, Mater. Sci. Eng., A **229**, 23 (1997).
[36] R. Doherty, D. Hughes, F. Humphreys, J. Jonas, D. Jensen, M. Kassner, W. King, T. McNelley, H. McQueen, and A. Rollett, Mater. Sci. Eng., A **238**, 219 (1997).
[37] D. A. Hughes, D. C. Chrzan, Q. Liu, and N. Hansen, Phys. Rev. Lett. **81**, 4664 (1998).
[38] M. Ortiz and E. A. Repetto, J. Mech. Phys. Solids **47**, 397 (1999).
[39] A. Argon and P. Haasen, Acta Metall. Mater. **41**, 3289 (1993).
[40] M. Zehetbauer, Acta Metall. Mater. **41**, 589 (1993).
[41] M. Zehetbauer and V. Seumer, Acta Metall. Mater. **41**, 577 (1993).
[42] P. Les, M. Zehetbauer, and H. Stuwe, Phys. Status Solidi A **157**, 265 (1996).
[43] M. J. Cawkwell, T. D. Sewell, L. Zheng, and D. L. Thompson, Phys. Rev. B **78**, 014107 (2008).
[44] P. Franciosi, M. Berveiller, and A. Zaoui, Acta Metall. **28**, 273 (1980).
[45] P. Franciosi and A. Zaoui, Acta Metall. **31**, 1331 (1983).
[46] A. M. Cuitiño and M. Ortiz, Eng. Comput. **9**, 437 (1992).
[47] T. Y. Wu, J. L. Bassani, and C. Laird, Proc. R. Soc. London, Ser. A **435**, 1 (1991).
[48] J. L. Bassani and T. Y. Wu, Proc. R. Soc. London, Ser. A **435**, 21 (1991).
[49] G. R. Piercy, R. W. Cahn, and A. H. Cottrell, Acta Metall. **3**, 331 (1955).
[50] R. J. Asaro, Adv. Appl. Mech. **23**, 1 (1983).
[51] P. Xu, S. Zybin, S. Dasgupta, and W. A. Goddard III (private communication).
[52] M. Ortiz, E. A. Repetto, and L. Stainier, J. Mech. Phys. Solids **48**, 2077 (2000).
[53] S. Aubry and M. Ortiz, Proc. R. Soc. London, Ser. A **459**, 3131

(2003).
[54] S. Conti and M. Ortiz, Arch. Ration. Mech. Anal. **176**, 103 (2005).
[55] S. Conti and F. Theil, Arch. Ration. Mech. Anal. **178**, 125 (2005).
[56] S. Conti, G. Dolzmann, and C. Klust, Proc. R. Soc. London, Ser. A **465**, 1735 (2009).
[57] N. Albin, S. Conti, and G. Dolzmann, Proc. - R. Soc. Edinburgh, Sect. A: Math. **139**, 685 (2009).
[58] G. Dal Maso, *An Introduction to* Γ*-Convergence* (Birkhauser, Boston, 1993).
[59] B. Dacorogna, *Direct Methods in the Calculus of Variations* (Springer, New York, 1989).
[60] S. Müller, *Calculus of Variations and Geometric Evolution Problems* Lecture Notes in Mathematics Vol. 1713, edited by S. Hilderbrandt and M. Struwe (Springer-Verlag, New York, 1999), pp. 85–210.
[61] R. J. Caspar, J. M. Powers, and J. J. Mason, Combust. Sci. Technol. **136**, 349 (1998).
[62] J. M. Powers, Combust. Theory Modell. **3**, 103 (1999).
[63] J. B. Ramsay and A. Popolato, *Proceedings of the Fourth Symposium (International) on Detonation*, edited by S. J. Jacobs (1965), pp. 233–238.
[64] A. Braides and A. Defranceschi, *Homogenization of Multiple Integrals* (Oxford University Press, USA, 1998).
[65] S. Conti, P. Hauret, and M. Ortiz, Multiscale Model. Simul. **6**, 135 (2007).
[66] M. Fago, Ph. D. thesis, California Institute of Technology, Pasadena, California (2004).
[67] H. G. Gallagher, P. J. Halfpenny, J. C. Miller, and J. N. Sherwood, Philos. Trans. R. Soc. Lond. **339**, 293 (1992).
[68] P. J. Halfpenny, K. J. Roberts, and J. N. Sherwood, J. Mater. Sci. **19**, 1629 (1984).
[69] J. J. Mason, A. J. Rosakis, and G. Ravichandran, Mech. Mater. **17**, 135 (1994).
[70] J. Hodowany, G. Ravichandran, A. J. Rosakis, and P. Rosakis, Exp. Mech. **40**, 113 (2000).
[71] P. Rosakis, A. J. Rosakis, G. Ravichandran, and J. Hodowany, J. Mech. Phys. Solids **48**, 581 (2000).
[72] Q. Yang, L. Stainier, and M. Ortiz, J. Mech. Phys. Solids **54**, 401 (2006).
[73] L. Stainier, A. M. Cuitiño, and M. Ortiz, J. Mech. Phys. Solids **50**, 1511 (2002).
[74] J. K. A. Amuzu, B. J. Briscoe, and M. M. Chaudhri, J. Phys. D **9**, 133 (1976).
[75] J. M. Winey and Y. M. Gupta, J. Appl. Phys. **90**, 1669 (2001).
[76] H. H. Cady and A. C. Larson, Acta Crystallogr., Sect. B: Struct. Crystallogr. Cryst. Chem. **31**, 1864 (1975).
[77] I. J. Dagley, R. B. Parker, D. A. Jones, and L. Montelli, Combust. Flame **106**, 428 (1996).
[78] R. N. Rogers, Thermochim. Acta **11**, 131 (1975).
[79] R. L. Gustavsen, S. A. Sheffield, and R. R. Alcon, J. Appl. Phys. **99**, 114907 (2006).
[80] R. E. Winter, S. S. Sorber, D. A. Salisbury, P. Taylor, R. Gustavsen, S. Sheffield, and R. Alcon, Shock Waves **15**, 89 (2006).
[81] P. A. Urtiew and C. M. Tarver, Combust., Explos. Shock Waves **41**, 766 (2005).
[82] J. J. Dick, C. A. Forest, J. B. Ramsay, and W. L. Seitz, J. Appl. Phys. **63**, 4881 (1988).
[83] S. A. Sheffield and R. Engelke, in *Shock Wave Science and Technology Reference Library*, edited by Y. Horie (Springer-Verlag, New York, 2009), Vol. 3, Chap. 1, pp. 1–64.
[84] P. A. Urtiew, K. S. Vandersall, F. Tarver, C. M. Garcia, and J. W. Forbes, Russ. J. Phys. Chem. B **2**, 162 (2008).
[85] P. A. Urtiew, J. W. Forbes, C. M. Tarver, K. S. Vandersall, F. Garcia, D. W. Greenwood, P. C. Hsu, and J. L. Maienschein, in *Shock Compression of Condensed Matter*, AIP Conf. Proc. No. 706, edited by M. N. Furnish, Y. M. Gupta, and J. W. Forbes (AIP, New York, 2004), pp. 1053–1056.
[86] R. L. Rabie and H. H. Harry, Los Alamos National Laboratory Techical Report No. LA-UR-92-1928, 1992.
[87] N. K. Bourne and J. E. Field, Proc. R. Soc. London, Ser. A **455**, 2411 (1999).